ORIGINAL RESEARCH ARTICLE

Cu-Doped and Un-Doped WO$_3$ Photochromic Thin Films

Yazan Badour[1] · Sylvain Danto[1] · Christine Labrugère[1] · Matthieu Duttine[1] · Manuel Gaudon[1]

Abstract

In this work, 0%, 0.5%, 1%, and 2% Cu-doped WO$_3$ nanoparticles were synthesized via a polyol method. The as-synthesized materials were characterized by x-ray diffraction, scanning electron microscopy (SEM), electron paramagnetic resonance (EPR), x-ray photoelectron spectroscopy (XPS), and UV-Vis photochromic activity. A bond valence model was adopted to explain the relationship between the lattice parameter and Cu percentage. Additionally, two films (1% Cu-doped and un-doped samples) obtained by dip-coating from a well-dispersed suspension were optically investigated using ex situ and in situ UV-Vis spectrometry; coloring/bleaching kinetics were thoroughly studied. The Cu-doped WO$_3$ film was found to have a high-quality bleaching mechanism (five times as fas as the un-doped WO$_3$ film). Finally, the high bleaching performance of the doped films was confirmed by successive cycling, showing that the as-prepared compounds are of great interest for smart window applications, for example.

Keywords Photochromism · redox · semiconductors · tungsten oxide · nanoparticles · polyol synthesis

Introduction

Tungsten oxide compounds (WO$_x$) have been intensively investigated over the past few decades due to their large variety of structures giving rise to great potential applications such as photochromic optical devices, gas sensors, photocatalysts, flat panel displays, and in field emission.[1–3] WO$_3$ is an n-type indirect-bandgap semiconductor with an optical bandgap ranging from 2.7 eV to 3.25 eV, which allows UV-light absorption.[4] Pristine WO$_x$-based materials have good photochromic behavior, but this intrinsic property has several limitations, including its limited applicable wavelength range, poor reversibility, and low photoresponse kinetics.[5,6] Because of these drawbacks, considerable attention has been directed towards composite inorganic materials due to their improved performance based on synergistic effects.[7] In another approach, doping the WO$_3$ crystalline structure with typical elements such as Al, Cu, Mo, Zn, and Co was investigated.[8–10] This was shown to decrease the oxide bandgap and especially, by introducing a narrow electronic band between the conduction band (CB) and the valence band (VB), to allow for the tuning of the photochromic UV irradiation response. Recently, in 2021, Dong's group conducted a detailed study on the effect of Cu doping on the photochromic properties of Cu@h-WO$_3$/WO$_3$·nH$_2$O hierarchical microsphere composites, where the self-bleaching process was shown to be greatly accelerated upon increasing the Cu doping concentration.[11] Shen et al.[12] found that the WO$_3$ photochromic behavior was greatly improved by Al^{3+} upon the formation of W$_2$O$_5$, which induced an electronic transition band between the VB and CB of WO$_3$, generating a red shift of the gap values and leading to strongly enhanced photochromic performance of WO$_3$. Also, the electronic, catalytic and optical performance of WO$_3$ can be enhanced by refining the oxide crystallite size and chemical purity.[13] Thus, diverse chemical synthesis methods have been adopted for preparing pure nano-WO$_3$ including hydrothermal,[14] sol–gel[15] and polyol methods.[16]

As was reported in our previous work,[17] the WO$_{3-x}$ nanoparticles (NPs) prepared by the polyol method demonstrated improved chemical, morphological, structural, and optical properties, including improved photochromic behavior. This encouraged us to conduct a detailed photochromic (coloring or bleaching cycles) study on thin films obtained by dip-coating from non-stoichiometric WO$_{3-X}$ NPs in suspension.[18] In this latest study, we found that the photochromism

✉ Manuel Gaudon
manuel.gaudon@icmcb.cnrs.fr

1 CNRS, Institut de Chimie de La Matière Condensée de Bordeaux, UMR 5026, University Bordeaux, 33600 Pessac, France

phenomenon was based on two kinetic components, the photoreduction of W^{6+} ions in W^{5+} defects at the particle surfaces, and the diffusion of the W^{5+} species within the bulk of the particles, which led to a coloration mechanism from the W^{5+}-W^{6+} intervalence charge transfer (IVCT). Regardless of the improved optical contrast, the time necessary for a complete return seemed very long and needs to be improved. Hence, this limitation motivated us to search for another way to improve the photochromic performance of WO_{3-X} NP-based materials. In this context, we propose in this article to study the photochromic behavior of Cu-doped WO_3 thin film obtained by dip-coating of Cu-doped WO_{3-x} NPs dispersed in ethanol suspensions. In the first part, the discussion focuses on the effect of the different concentrations of Cu (0.5 mol%, 1 mol% and 2 mol%) introduced in the WO_{3-X} NPs prepared by the polyol method. In a second part, the photochromic (coloring and bleaching) behaviors of the doped and pristine films are compared and comprehensively analyzed.

Experimental

Polyol Synthesis of WO₃ Powders

Chemical reagents were purchased from Sigma-Aldrich and used as received. Tungsten(VI) chloride was used as the tungsten source, copper(II) chloride as the doping source, and diethylene glycol (DEG) as solvent. WCl_6 (7.2 g) was added to 100 mL of DEG and 20 mL of distilled water. The mixture was heated at 180°C under continuous stirring and refluxed for 3 h. At the end of the reaction, a deep blue precipitate was obtained. The precipitate was washed and centrifuged several times with ethanol to remove any traces of solvent and dried in an oven at 80°C before being washed in HCl solution (1 mol L^{-1}) for surface functionalization with protons.

In this way, a series of Cu-doped-WO_3 samples were prepared while varying the Cu concentration from 0%, 0.5%, 1%, and 2% and were labeled WO, WCu05, WCu1, and WCu2 for raw powders, respectively. In another batch, the as-synthesized powders (0%, 0.5%, 1%, 2% Cu) were annealed at 600°C under an air atmosphere for 2 h and were labeled WOT, WCuT05, WCuT1, and WCuT2, respectively.

Pristine and Doped Film Elaboration

The pristine WO and WCu1 raw NPs were separately dispersed in ethanol to prepare the suspensions (weight content in NPs 90 g L^{-1}); then the suspensions were dip-coated on a standard glass substrate to obtain the pristine and doped thin films. The dip-coating parameters were as follows: (i) dip-coating speed of 133 mm min^{-1}, and (ii) for multilayers,

successive dip-coating steps, with drying in an oven (90°C) for 30 min between steps.

Characterization Techniques

Powder Characterization

The crystal structure characterization of the products was performed by x-ray diffraction (XRD) analysis (PANalytical X'Pert Pro, Cu $K_{\alpha 1}$ = 1.54056 Å, $K_{\alpha 2}$ = 1.54439 Å and 2θ range from 8° to 80°). The unit cell parameters were refined by structural pattern matching using the FullProf program. The surface morphology of the samples was investigated by scanning electron microscopy (FEI Quanta 3D FEG) working at 5 kV acceleration voltage.

To detect Cu^{2+} ($3d^9$) and W^{5+} ($5d^1$) paramagnetic ions and/or free electrons in the CB of the tungsten trioxide semiconductors, electron paramagnetic resonance (EPR) experiments were performed on powder samples. EPR spectra were recorded from room temperature down to 4 K with a Bruker ESP300E spectrometer equipped with a liquid helium flow cryostat. In addition, 9.54 GHz (X-band) microwaves with 50 mW power and 100 kHz magnetic field modulation with 0.5 mT amplitude were used for these experiments. The magnetic field (and g-value) scale was calibrated with a DPPH ((2,2)-diphenyl-1-picrylhydrazyl; g = 2.0036) reference sample. The analysis of the EPR spectra was performed with Bruker WinEPR and WinSimfonia software.

The optical properties of the resulting products were tested by UV–Vis diffuse reflectance spectroscopy at room temperature from 200 nm to 2000 nm with a Varian Cary 5000 spectrometer using an integration sphere (spectral resolution: 1 nm and band length: 2 nm). Halon was used as white reference. RGB space colorimetric parameters were determined from the spectra using a two-step mathematical treatment. The first step consists in extracting the XYZ tri-stimulus values (defined by the CIE 1964) from the integration (over the visible range, i.e. from λ = 380 nm up to 780 nm) of the product of x(λ), y(λ) or z(λ) functions (CIE 1964) with the diffuse reflectance spectra function $X = \int x(\lambda).R(\lambda).d\lambda$. Then, we used the transfer equations defined by CIE 1976 to transform the XYZ space to the L*, a* and b* common three-color space parameters.

A Thermo Fisher Scientific K-Alpha spectrometer was used for x-ray photoelectron spectroscopy (XPS) surface analysis with a monochromatized Al K_α source (hν = 1486.6 eV) and a 400-micron x-ray spot size. Pressure of 10^{-7} Pa was reached in the chamber when transferring the powders pressed onto indium foil. The full spectra (0–1100 eV) were obtained with constant pass energy of 200 eV and high-resolution spectra with constant pass energy of 40 eV. Charge neutralization was applied during analysis. High-resolution

spectra (i.e. C_{1s}, O_{1s}, W_{4f}) were quantified and/or fitted using the Avantage software provided by Thermo Fisher Scientific.

Film Characterization

Dynamic light scattering (DLS) was used to determine the size distribution profile of the pristine and doped NPs in the suspensions used for dip coating process with a VASCO™ nanoparticle size analyzer. The transmission spectra of the films were recorded at room temperature from 200 nm to 2500 nm on a Varian Cary 5000 spectrophotometer. The irradiation conditions were achieved using a UV Hg-lamp (Vilber Lourmat 8.LC) at a monochromatic wavelength of 365 nm. The film was placed at 10 cm from 8 W tubes: the power per surface unit received by the sample is equal to 5.6 W/m², i.e., irradiance close to the UV-daylight irradiance in London daylight. The use of such low fluence is to mimic the real conditions to which a smart device (window or textile) is exposed to in daylight. Self-bleaching occurred naturally after samples were placed in a dark room away from light. Finally, the thickness of the films was determined using a Wyko NT1100 optical profilometer.

Results and Discussion

Powder Physicochemical Characterization

The structure of the as-prepared powders was characterized by XRD. No second phase corresponding to impurities such as Cu, Cu_2O or CuO was detected in the x-ray patterns for any of the samples. The XRD diagrams show that all raw powders, WO, WCu05, WCu1 and WCu2, were crystallized with a cubic Pm-3m structure (Fig. 1a),[17] and Fig. 1b shows the powders obtained after post-annealing under air, with a P21/n monoclinic structure. The very large peaks associated with the nanometric behavior of the raw powders do not allow their fitting for accurate structural characterization. Thus, to determine the impact of the copper content introduced inside the WO₃ crystalline framework, especially on crystallite size and the unit-cell lattice parameters, pattern-matching refinement of the air-annealed powders was performed, as shown in Fig. 1b. The pattern matching of the air-annealed samples was achieved using the P21/n space group. The matching quality was good, and the reliability factors were far below 10%: for example, Rexp =
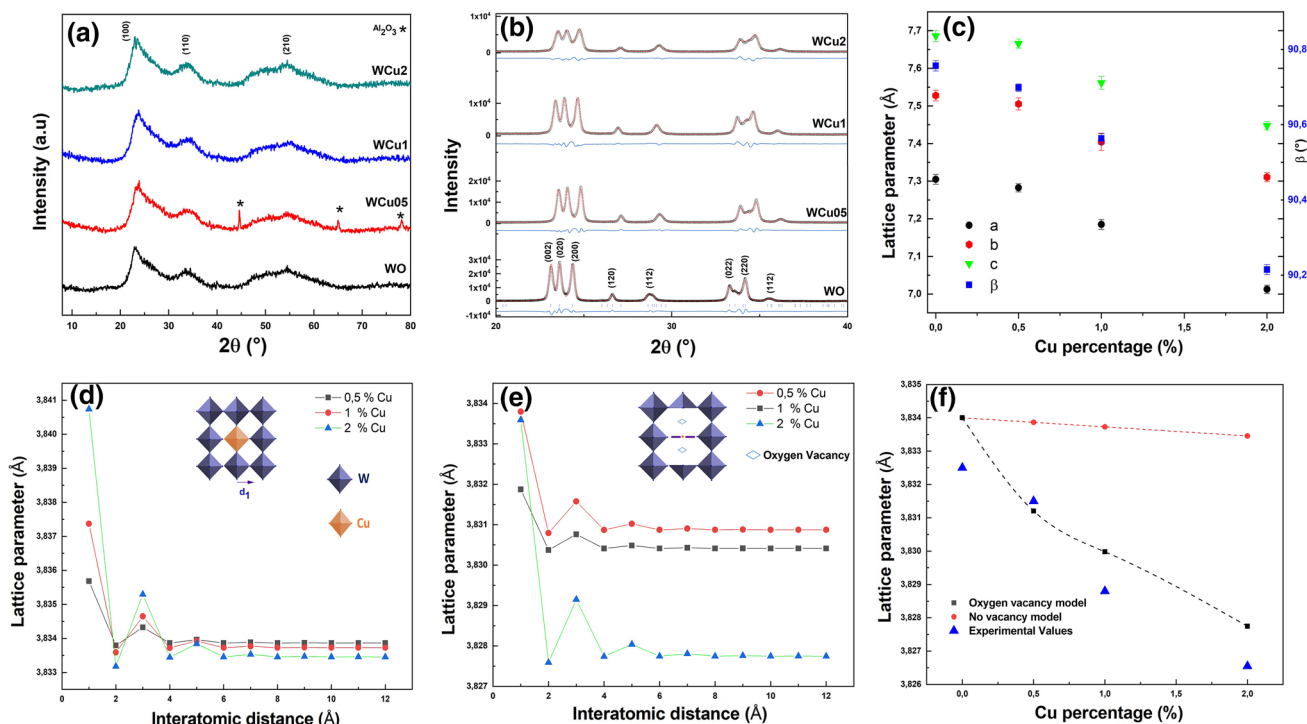
Fig. 1 XRD pattern of un-doped and Cu-doped WO₃ raw powders (a). XRD with pattern matching refinement for un-doped and Cu-doped WO₃ annealed powders under air at 600°C (b). Evolution of un-doped and Cu-doped WO₃ annealed powder lattice parameters as a function of Cu dopant percentage (c). Calculation of the Cu doping effect on the Cu-doped WO₃ pseudo-cubic lattice parameter considering W^{6+} for Cu^{2+} substitution without electronic compensation versus length of the coordination sphere number around copper taken for calculation (d). W^{6+} for Cu^{2+} substitution with double oxygen vacancy creation for electronic compensation (e). Calculated and experimental lattice parameter values (f).

2.16%; Rf = 6.55%; Rp = 8.47% for the WOT compound. From the diffraction pattern peak profiles, it was possible to determine the average crystal size of the particles using the Debye-Scherrer formula,[19] $t = K.\lambda / (\beta.\cos\Theta)$, where t is the mean size of the ordered (crystalline) domains, which may be smaller than or equal to the particle size, K is the proportionality factor (also called the Scherrer constant), whose value is often assumed to be $K = 0.9$, β is the full width at half maximum (FWHM), λ the x-ray wavelength, and θ the Bragg angle. It should be noted that the observed peak width is affected by the instrumental broadening as well as the broadening caused by the size effect (size broadening), so the instrumental broadening is subtracted from the total peak width to calculate the crystallite size.

The nanometric sizes were calculated as (i) 5.5 nm, 3.2 nm, 3.5 nm, and 2.6 nm for WO, WCu05, WCu1, and WCu2, respectively, and (ii) 25.6 nm, 22.34 nm, 19.8 nm, and 21.8 nm for WOT, WCuT05, WCuT1, and WCuT2, respectively. The copper doping, especially for the post-annealed samples, led to a decrease in the average particle size, which argues for an efficient introduction of the copper ions inside the WO_3 crystalline framework. As shown in Fig. 1b, the decrease in the crystallite size is associated with the decrease in the intensity of the major diffraction peaks (020), (002), and (200) with the increase in Cu concentration. This trend can be attributed to the formation of the copper ion clusters and crystal defects, which can limit the growth of the Cu-coped WO_3 NPs.[20] Furthermore, the incorporation of Cu ions into the WO_3 crystal affected the lattice parameters of Cu-doped WO_3, as the Cu^{2+} ions and W^{6+} ions have different ionic radii, which are 7.3 and 6.0 Å in 6-coordinated spheres, respectively, as well as different oxidation states (aliovalent doping). Rietveld refinement performed on the Cu-doped samples did not reveal any electronic residues in the interstitial position (e.g., in the icosahedral sites, which are known to be preferential locations for alkaline dopants in a WO_3-type framework[21]). Hence, in the following, the copper ions are considered in substitution for the tungsten ions. Additionally, the copper oxidation states are assumed to be +II, which will be supported by further EPR experiments.

As illustrated in Fig. 1c, further analysis on the monoclinic lattice parameters (a, c, and β angle) of Cu-doped samples shows a clear and monotonic decreasing trend as the Cu doping concentration increases. This observation could constitute an interesting paradox as the Cu^{2+} ionic radius is over the W^{6+} radius. The evolution of the unit-cell lattice parameters was interpreted with respect to the bond valence model.[22] However, two different approaches were applied to better understand the evolution of the Cu-doped WO_3 lattice parameters upon doping with Cu. First, for simplification, the evolution of the unit-cell parameters was resumed to the pseudo-cubic a unit-cell parameter (considering the equivalent cubic cell with Z, the number of WO_3 unit per cell,

equal to unity). In a rough model, in a first approximation, a pseudo-cubic lattice parameter was calculated taking into consideration a W^{6+} for Cu^{2+} substitution without electronic compensation. In a more accurate model, the creation of a double oxygen vacancy creation for electronic compensation is taken into account. For the calculation, the two oxygen vacancies are created along the z-axis, in first neighboring of the introduced copper ions, i.e., considering that copper II ions are so located in a regular square plane sites (in good agreement with the $3d^9$ Cu^{2+} electronic configuration).

In both approaches, the bond valence model of Brown et al.[22] was used to predict from geometrical modeling the drastic modifications of the W-O interatomic distances around the Cu^{2+} defect points. Indeed, the bond valence law states that the bond length (r_i), the coordination number (n), the electrostatic flux on each bond (v_i), and the ion oxidation state (or total ion valence: V) are all linked by Eq. 1:

$$V = \sum_{i=0}^{n} v_i = \sum_{i=0}^{n} \exp\big((r_0 - r_i)/0.37\big) \tag{1}$$

where V is the valence of the ion (equal to the oxidation degree modulus: here = 6 for W^{+6}, 2 for Cu^{2+}), v_i is the bond valence of each bond implying the central ion, r_0 is an empirically determined parameter characteristic of the A−X bond (r_0 is tabulated equal to 1.917 Å, and 1.679 Å for Cu^{2+}−O^{2-} bond), and r_i is the length of each i bond of the first coordination sphere.

This model is very effective for explaining that aliovalent doping by a low-valence but larger-radius ion could paradoxically lead to a decrease in the unit-cell parameters, exactly as observed for Cu-doped WO_3 samples. Indeed, even if the Cu-O bonds are longer than the standard W-O bonds, the increase in the electronic flux of the W-O bonds at the proximity of the copper defect leads to a contraction of these W-O bond lengths. The surrounding crystalline network around the copper defect must compensate the low electronic flux between oxygen and copper, because the total valence of the Cu-bonded oxygen anions equal to 2 must remain constant.

In addition, we use Vegard's law (a mixing law) to evaluate the lattice parameter, taking into account the valence bond modification from neighbor to near-close bond fluxes up to the tenth coordination sphere from copper ions.[23] For the first model, the lattice parameter remains the same for all three axes, whereas in the second model, for which a double oxygen vacancy (V_O) was introduced along the z axis, the lattice parameter on z axis a_z differs from the x and y axes ($a_x = a_y \neq a_z$). Then the average calculated pseudo-cubic unit-cell parameter a is taken as $a = (a_x \cdot a_y \cdot a_z)^{1/3}$. Thus, for both the first and the second model, a pseudo-cubic parameter for x copper concentration (n being the number of coordination spheres around copper taken in the model) can

be calculated from Eqs. 2 and 3. The two models diverge in the way to calculate near-close bond fluxes.

$$a_n = 2.d_{(W-O)}(1-2x) + 2.x.d_{(Cu-O)} + \sum_{(i=0)}^{(i=n)} 2.x.d_i \qquad (2)$$

$$\text{with} \quad d_i = r_{0(W/Cu-O)} - 0.37.\ln(v_i) \qquad (3)$$

The final calculation for the two models is represented in Fig. 1d and e, respectively, for non-vacancy approximation and double oxygen vacancy approximation. The second applied model is in good accord with the experimental values, which confirms that substituting W^{6+} by Cu^{2+} causes a decrease in the lattice parameters and leads to shrinkage of the unit cell. The fact that the second model leads to calculation so close to the experimental values indicates that compensation of copper doping with a double oxygen

vacancy is a convenient way to confirm the evolution of lattice parameters.

The sample morphologies are reported in the SEM images in Fig. 2. As shown in Fig. 2a–d, the raw sample particles are very small, around 3 nm. The crystallite size distribution extracted from SEM image treatment is reported in Fig. 1i. All the doped and un-doped NPs have almost a superimposed particle size distribution. This very small size is in good agreement with the previous discussion extracted from the XRD patterns. The air-annealed powders show significantly larger isotropic particles of about 50 nm average diameter (Fig. 2e–h). However, the doped NPs do not exhibit a change in their morphology and size distribution in comparison with the un-doped NPs. The decrease in the coherent domain with the copper concentration shown from x-ray patterns is not confirmed. It is possible that the slight enlargement of the peak width versus copper content observed in XRD comes more from constraints created from copper
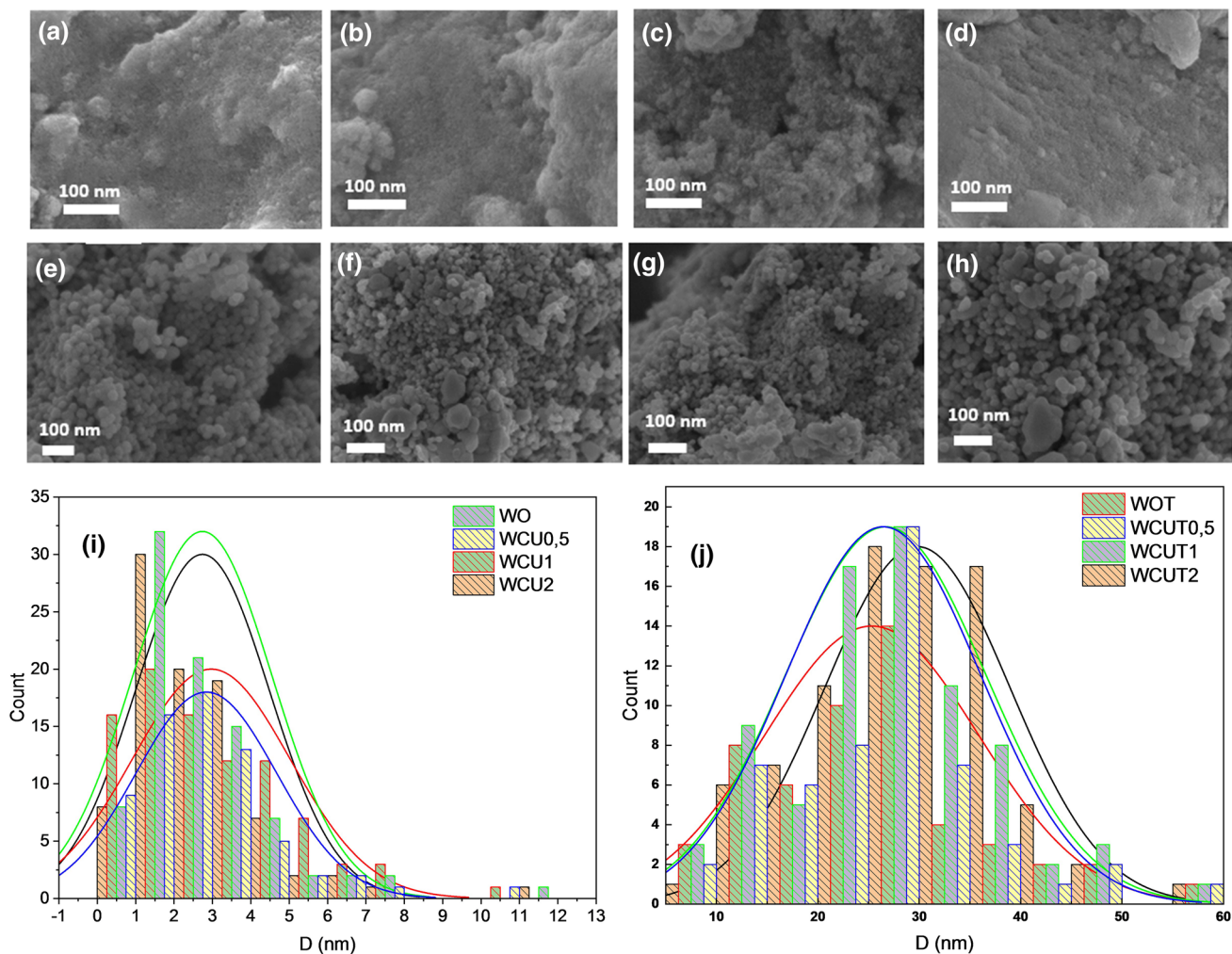
Fig. 2 SEM images of the various raw and post-annealed samples: WO (a), WCu05 (b), WCu1 (c), WCu2 (d), WOT (e), WCuT05 (f), WCuT1 (g), WCuT2 (h), and their associated particle size distribution (i and j).

introduction than from a decrease in the average crystallite size. As the monoclinic samples were comprehensively analyzed in terms of XRD to confirm the substitution of tungsten cation for copper due to their well-defined XRD patterns, in the following study, we will focus on the raw powders, as these samples are the only ones exhibiting the target photochromic properties.

In order to reveal the presence of conduction electrons and to track the variation in Cu^{2+} and W^{5+} content within the studied products, EPR experiments were performed from room temperature down to 4 K (Fig. 3). First, no conduction electron, responsible for a sharp and intense signal with g factor close to free electron g value ($g_e = 2.0023$), was detected in any of the analyzed samples. However, the EPR spectra of Cu-doped WO_3 powders mainly exhibit an axial signal ($g_\perp = 2.085$ and $g_{//} = 2.42$) with a hyperfine structure ($A_\perp \approx 2$ mT and $A_{//} = 12$ mT) whose intensity increases linearly with the Cu-doping rate. This EPR signal with $g_{//} > g_\perp > g_e = 2.0023$ is characteristic of $3d^9$ Jahn-Teller Cu^{2+} ions ($S = 1/2$ and $I = 3/2$ for ^{63}Cu and ^{65}Cu isotopes) located in tetragonally distorted octahedra (D_{4h} local symmetry). Clearly, the experiment shows that copper is well introduced in the WO_3-type crystalline structure and with mainly the +II oxidation number. Nevertheless, the presence of copper ions at a lower oxidation state may not be rejected as diamagnetic Cu^+ ($3d^{10}$) is EPR silent.[24] Moreover, low-temperature EPR spectra show at higher magnetic
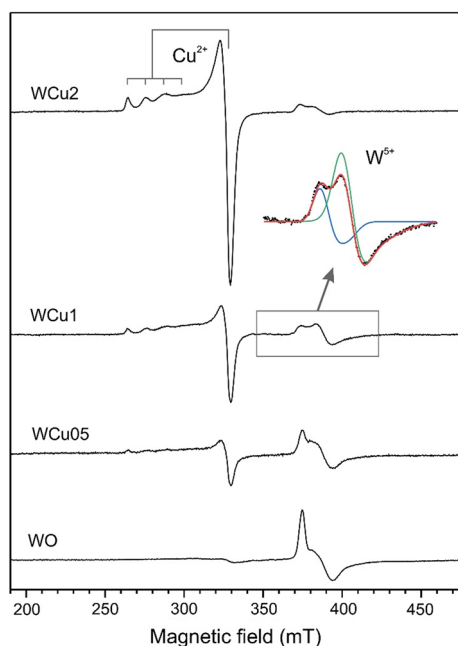
field two additional signals associated with $5d^1$ W^{5+} ions (Fig. 3). These apparently axial signals (inset of Fig. 3) with g values $g_{zz} = 1.82$, $g_{yy} = 1.80$, $g_{xx} = 1.76$ and $g_{zz} = 1.77$, $g_{yy} = 1.74$, $g_{xx} = 1.69$ can be attributed to slightly different local environments for fivefold coordinated W^{5+} ions (with a symmetry close to C_{4v}) and then to the occurrence of oxygen vacancies within all the analyzed samples.[25] The presence of W^{5+} ions in the raw powder can be easily explained by the reducing medium used during the polyol synthesis process, which resulted in an oxygen sub-stoichiometry with chemical formulae WO_{3-x}. Two observations can be made with regard to W^{5+} signals versus copper concentration: (i) the intensity of the signal progressively decreases, showing that copper insertion plays an oxidative role besides tungsten ions; (ii) the ratio between the two W^{5+} signals clearly evolves, showing the perturbation of the W^{5+} local environments.

XPS was used to analyze the surface composition as a complementary analysis technique to EPR. Indeed, a clear picture of the tungsten oxidation states could be achieved, whereas EPR was obviously insensitive to the W^{6+} diamagnetic cations. Furthermore, the environment of the oxygen anions in the powders, especially the ability to distinguish oxygen anions in a bulk environment from those perturbed by oxygen vacancies, is very useful for materials understanding.

Firstly, the XPS spectra of two air-annealed compounds, the un-doped (WO) and the 2 mol% Cu-doped sample (WCuT2), are compared. Figure 4a shows that the air annealing post-treatment produced full oxidation of the tungsten ions up to the +VI oxidation state in the WOT samples. Indeed, the WOT spectrum comprises only two peaks, which were assigned without any doubt to the W^{6+} state ($4f_{5/2}$ and $4f_{7/2}$ doublet at 38.0 eV and 35.9 eV).[26] This sample is thus a reference demonstrating that no further reduction of W^{6+} to W^{5+} is occurring during the XPS spectrum acquisition. However, the W_{4f} fitting of the air-annealed WCuT2 shows a residual signal of W^{5+}. The W^{5+} doublet, $4f_{5/2}$–$4f_{7/2}$: 36.8–34.6 eV, confirms the substitution of tungsten ions by the Cu^{2+}. Indeed, W^{5+} may be created from a redox reaction proceeding from IVCT between W^{6+} and Cu^{2+} cations, leading to W^{5+} and Cu^+ cations. Also, the occurrence of W^{5+} inside the WCuT2 compound is in coherence with the green color of the annealed powder compared to the yellow color of the un-doped WOT powder.

The other spectra all deal with un-doped or doped raw powders. Figure 4c shows the high-resolution fitting of W_{4f} spectra in the pure WO sample where the two major peaks were assigned to W^{6+} while the two minor peaks were assigned to W^{5+} cation. The W^{5+} state occurrence indicates the creation of oxygen vacancies as a result of a partial reduction of W^{6+} due to the reducing medium used during the polyol synthesis, as reported in our last paper.[27]

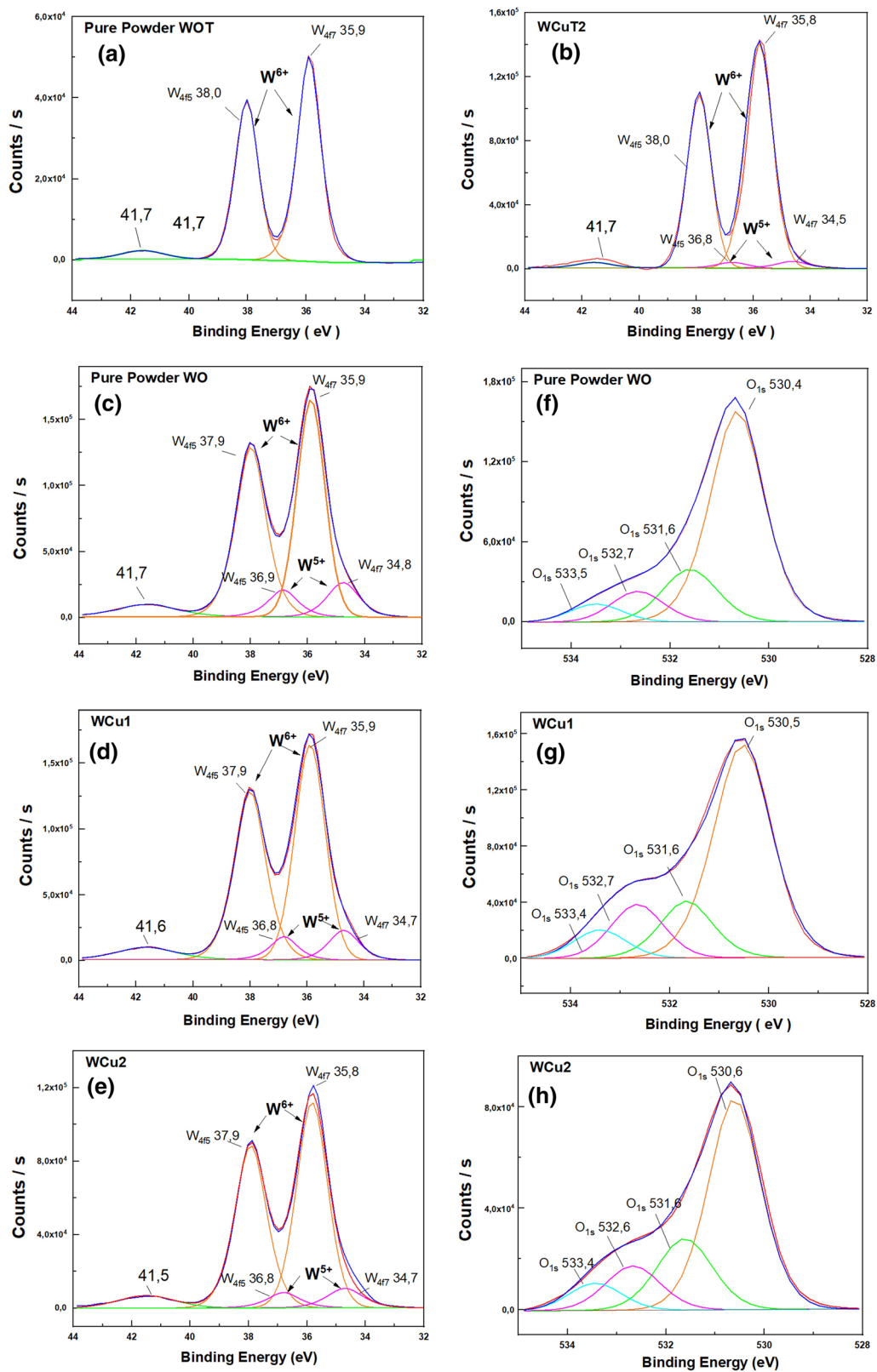
Fig. 3 Low-temperature (4 K) X-band EPR spectra of un-doped and Cu-doped WO_3 raw powders. The inset highlights the two distinct EPR signals associated with two different local environments for W^{5+} ions.

Fig. 4 High-resolution XPS spectra of W_{4f} (a–e) and O_{1s} (f, g, h) in WOT (a), WCuT2 (b). WO (c and f), WCu05 (d and g), WCu2 (e and h).

Therefore, the un-doped tungsten oxide NPs have an oxygen sub-stoichiometry with the formula: WO_{3-x}.

Similarly, the fitting of W_{4f} spectra for each of the raw Cu-doped WO_{3-x} samples revealed two W^{6+} and W^{5+} doublets.[28] Nevertheless, the ratio between the tungsten V and tungsten VI peaks is clearly decreasing versus the copper concentration. Hence, W^{5+} content in WO sample is calculated from $W4f_{7/2}$ peak area ratio, to be equal to 0.19 and was found to be decreased to 0.14 and 0.11 in WCu1 and WCu2, respectively.

For all the powders, the high-resolution O_{1s} spectra were fitted with four components to bring supplementary information. As shown in Fig. 4f–h, the strongest signal at 530.7 eV corresponds to the oxygen atoms contained in the stoichiometric structure of WO_3,[28,29] i.e., introduced in a well-defined 6-coordinated oxygen site. The second signal (531.7 eV) is related to the existence of oxygen defects in the sub-surface planes of the powders. The signal at 532.7 eV corresponds to oxygen bound to carbon atoms, which could come from the synthesis route (polyol-mediated precipitation), and the signal at 533.3 eV is attributed to water pollution. Interestingly, the peak intensity of O_{1s} state relative to oxygen defects (located at 531.7 eV) shows a significant increase upon Cu doping increase. This leads to an estimation of the oxygen vacancy (V_O), estimated from the O_{1s} 531.8 / O_{1s} 530.7 area ratio, content equal to 0.12 in the un-doped sample, and to 0.24, 0.32 in WCu1, WCu2, respectively. This last observation so indicates a drastic increase in the oxygen vacancies in WO_{3-x} after Cu doping, which could be due to the aliovalent character of the chemical doping. Indeed, the drastic difference in the valence state of the Cu ion with respect to the host W ions of the matrix should be electronically compensated from oxygen vacancies. This observation is in good agreement with the variation in the unit-cell parameters versus copper concentration which were discussed previously.

Powder Photochromic Properties

The optical photochromic response of the as-prepared powders under UV irradiation was studied on the whole UV–visible–near-infrared (NIR) range by measuring the diffuse reflectance spectra of the un-doped and doped raw powders. All samples were characterized before UV irradiation and after 5 min of irradiation, as shown in Fig. 5.

Firstly, the doped and un-doped powders possess total absorption in the UV, i.e., typically characteristic of a wide-gap semiconductor, with the gap being located at 420 nm for the un-doped and shifted to 485 nm for the doped powder. Furthermore, a quite important absorption in the visible and the NIR part of the spectrum is due to the IVCT between W^{5+} and W^{6+}, or can even be described from the creation of the free charge carriers in the CB associated with
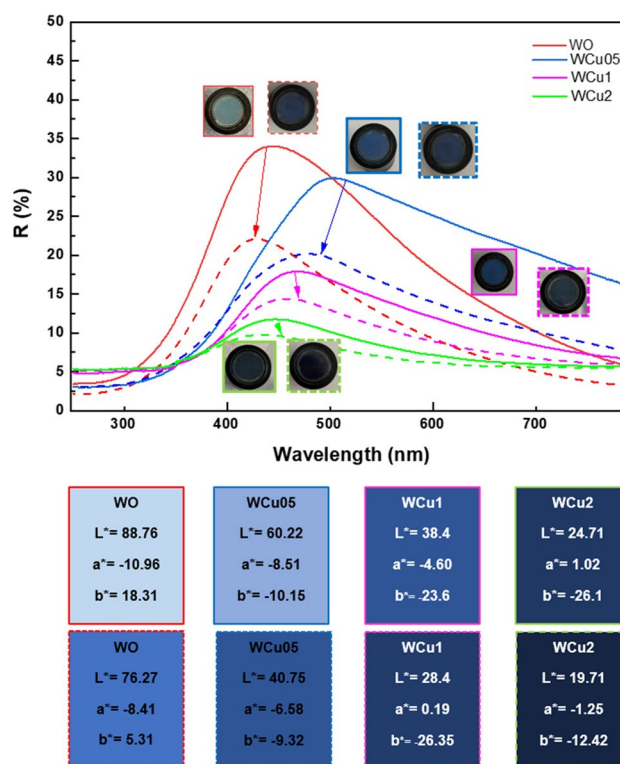
Fig. 5 Diffuse reflectance spectra of the un-doped and Cu-doped WO_3 raw powders and their associated L*, a*, b* parameters before irradiation (solid line) and after 10 min UV irradiation (dashed line).

the reduction of tungsten ions as explained by the Drude electron cloud theory.[7] For the non-irradiated compounds, the infrared absorption increases with the copper concentration. Because the W^{5+} ion concentrations were shown to decrease with the copper concentration, the increase in the intervalence transfer probability with copper supports the participation of the copper in electron mobility: the occurrence of multi-site charge transfers, as in the short chains $W^{5+}–Cu^{2+}–W^{6+} \rightarrow W^{6+}–Cu^{+}–W^{6+} \rightarrow W^{6+}–Cu^{2+}–W^{5+}$, can be explained by this phenomenon. Nonetheless, the oxygen sub-stoichiometry linked to the copper defects, as was confirmed by the XPS results, can also be at the origin of the absorption of more photons of the visible energy range. The maximum reflectivity percentage located at 480 nm decreases from 35% for the raw sample to 30% for the WCu05, to 17% for the WCu1 and 10% for the WCu2. As shown from the sample photographs as well as the reconstructed sample colorations from their L*, a*, b* colorimetric coordinates, the color of samples becomes darker upon increasing the copper concentration.

Irrespective of their copper doping attribute, all the samples exhibit a huge photochromism in comparison with previous investigations reported on WO_3 photochromism.[17,18] This behavior is related to the nanometric crystallite sizes. Indeed, thermodynamically, the relaxation of the steric constraints

linked to the photoreduction promoting the creation of new W^{5+} color centers would preferentially take place on oxide surfaces. Highly divided materials will then show improved photochromic properties.

The associated chromatic coordinates in the L*, a*, b* space presented in Fig. 5 allow for a comparison of the photochromic efficiency of the various samples from the optical contrast calculated between the non-irradiated samples and samples irradiated for 10 min. Indeed, even if our samples exhibit a photochromic effect mainly concentrated in the NIR part of the spectrum, the impact of the intervalence transfers in the visible range allows us to observe a visible ΔC contrast: $\Delta C = \sqrt{(\Delta b^{*2} + \Delta L^{*2} + \Delta a^{*2})}$. Photochromic contrasts are about 55.5, 50.6, 25.6, and 20.1 for WO, WCu05, WCu1, and WCu2, respectively. From the darkening of the non-irradiated compounds versus copper concentration, the copper introduction tends to decrease the powder photochromic efficiency in terms of optical contrast between bleached and colored states.

Thin Film Photochromic Properties

This section, which is devoted to the elaboration from powder to thin films and the characterization of its photochromic properties, is focused on the comparison between the un-doped tungsten oxide (WO) thin film and the 1 mol% Cu-doped WO₃ (WCu1) thin film.

The elaboration of good-quality thin films requires the elaboration of well-dispersed colloidal suspensions. DLS measurements were used to track the size variation of the 90 g L^{-1} dispersed NPs in suspension. Figure 6a shows that powder in ethanol suspension with a Gaussian particle size distribution from the WOCu1 powder (similar curve is obtained for the WO powder) with an average size equal to 23 nm is obtained from the adequate protocol already discussed in previous work.[18] The suspension remained stable, with no sedimentation observed over time.

Different films produced from successive dip-coating steps (with one, two, three, or four successive coated layers) were studied. The transmission spectra of the as-prepared thin films show good visible transmission with a very low scattering coefficient (Fig. 6b). The films show a maximum transmission equal to 80% at 600 nm, irrespective of the film thickness. However, a distinct low-intensity absorption band appearing at a wavelengths around 1200 nm is observed on the three- and four-layer films. This absorption band can be without any doubt attributed to the presence of W^{5+} ions due to the IVCT between W^{5+} and W^{6+} ions in the crystal network of the WO₃₋ₓ. The film thickness is plotted versus the number of deposited layers in Fig. 6c. The variation of the film thickness versus the number of coating layers is almost linear: about 100 nm thickness is achieved for each coating.
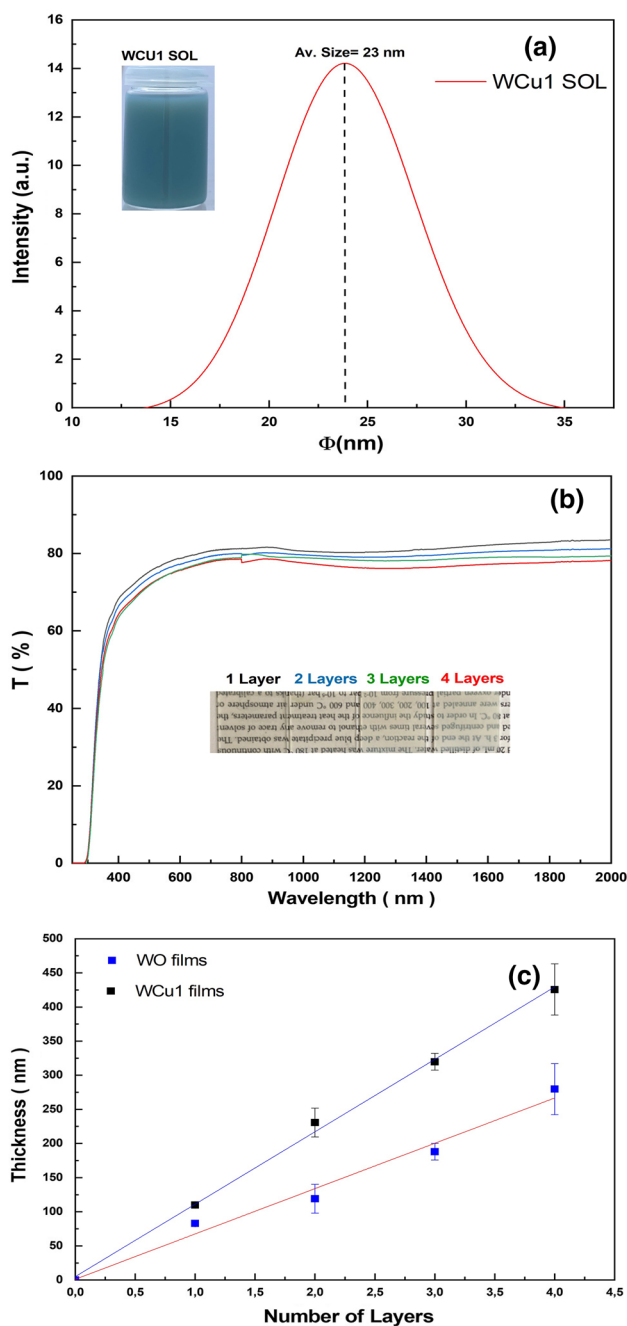
Fig. 6 Particle size distribution of WCu1 NPs in ethanol suspension (a), transmission electron spectra and photographs of WCu1 films with from one up to four successive dip-coated layers (b), evolution of raw and doped film thickness as a function of the number of dip-coated layers (c).

A preliminary photochromic test with fixed irradiation conditions (UV lamp, 8 W, 30 min) was conducted on all studied films. The test focused on the three-layer film, as significant IVCT was observed in the NIR region; these preliminary tests showed that UV irradiation is well able to generate a photochromism effect. Therefore, the

evolution of the spectrum of both WO and WCu1 films versus irradiation time was collected (Fig. 7a and b), and the evolution of the absorbance at 1.1 eV for WO films and 0.75 eV for WCu1 film was extracted to further investigate the photo-redox kinetic (Fig. 7c). As shown in Fig. 7a and b, the initial absorbance of the films (before UV irradiation) was considered as the reference absorbance (without any absorbance).

As seen from Fig. 7c, the absorbance at 1 eV (corresponding to the energy at which the IVCT band is greater) of the WO film seems to change rapidly in the first minutes of irradiation, then appears to slow beyond 15 min of irradiation until it is almost no longer evolving after 90 min. In turn, the absorbance of WCu1 appears to change more slowly than the WO in the first minutes of irradiation, then stabilizes after 90 min. Also, the absorbance band maximum is shifted at 0.75 eV. This change in position of the absorbance phenomenon is coherent with the participation of the Cu^{2+} to the IVCT (W^{6+} to W^{5+} via Cu^{2+} ions in intermediate positions) as a proposed mechanism to explain the darkening of the pristine oxide coloration before irradiation. To better express the differences between the two films, a double exponential function (a combination of two first-order kinetics laws) was used to fit the experimental data (absorbance evolution at its maximum), according to Eq. 4:

$$Y = A_1 \cdot \left[1 - \exp(-t/k_1)\right] + A_2 \cdot \left[1 - \text{ex}(-t/k_2)\right] \quad (4)$$

with t in minutes, and so two characteristic times (k_1 and k_2) in minutes, and two characteristic amplitudes (A_1 and A_2). The values of the four parameters are shown in Fig. 7c. For both films, the coloring kinetic involves two convoluted kinetic phenomena: a fast-kinetic component (k_1 is about 1 min), and a slow-kinetic component (k_2 is about 30 min). Hence, in both cases (doped or un-doped thin films), (i) the fast kinetic (during the very first minutes) could correspond to a quick photoreduction of the surface cations from W^{+6} to W^{+5}, and then, after a short time, the surface will be saturated with W^{+5} ions and this fast mechanism will stop; the slow kinetic could correspond to the ionic diffusion of the W^{5+} from the surface to the material bulk, allowing W^{5+} surface desaturation and thus new surface photoreduction. Nonetheless, a huge difference is observed between the doped and un-doped film: on the un-doped WO film, the coloring under UV irradiation is mainly governed by the fast kinetic phenomenon ($A_1 = 0.4$, where $A_2 = 0.17$), and the WCu1 film coloring is mainly governed by the diffusive slow kinetic ($A_1 = 0.0.4$, where $A_2 = 0.4$). The quasi-quenching of the fast kinetic originates in the defects associated with the Cu-doping. Basically, when the Cu atom takes the
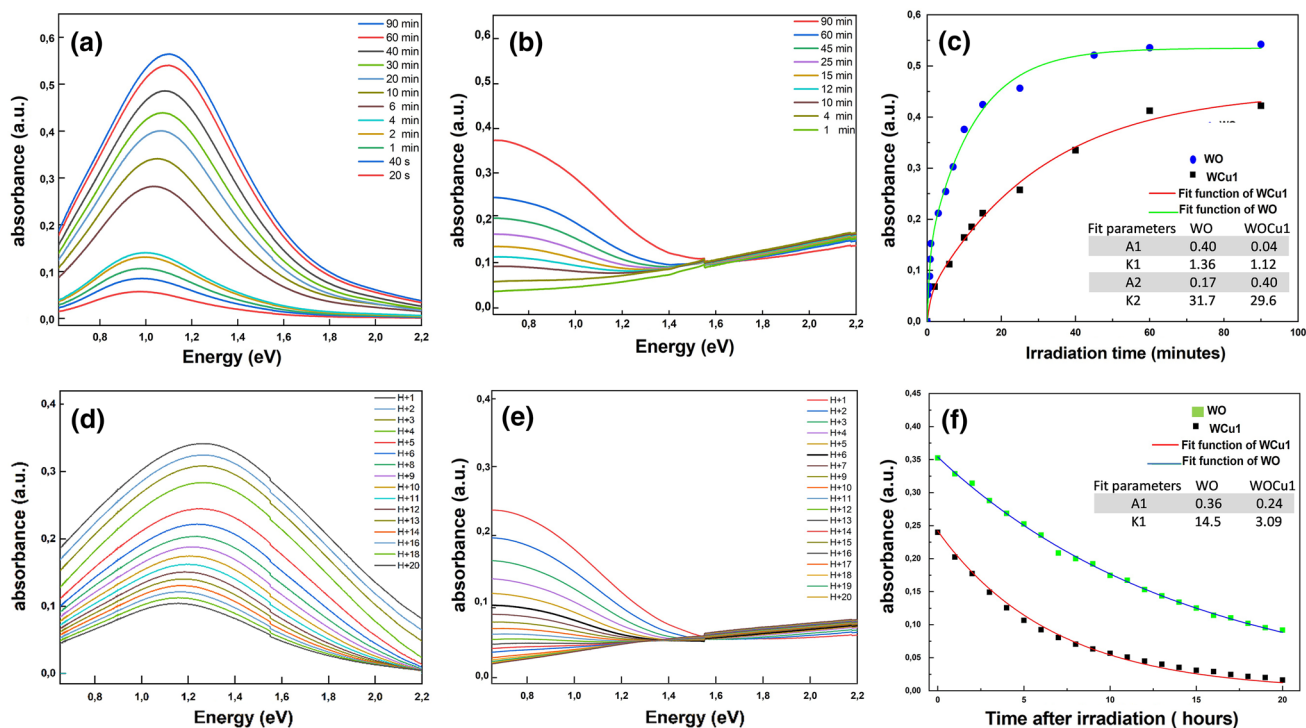
Fig. 7 Evolution of absorbance during irradiation (coloring) of WO film (a) and WCu1 film (b). For the two films, absorbance at 1 eV (WO) or 0.75 eV (WCu1) evolution versus irradiation time and the associated kinetic parameters (coloring kinetic) (c). Evolution of absorbance in dark conditions (bleaching) of WO film (d) and WCu1 film (e). For the two films, absorbance evolution at 1 eV (WO) film or 0.75 eV (WCu1) in dark conditions (bleaching kinetic) (f).

W site in WO$_3$, it produces three possible effects: (1) a narrowing of the fundamental bandgap of the system due to the strong d–p coupling between Cu and O, which in turn leads to an increased O 2p level, (2) the creation of an acceptor impurity narrow band above the VB of WO$_3$, which is formed by the empty Cu 3d (e$_g$) orbital, and (3) the creation of electronic compensating oxygen vacancies as bulk/surface defects.[30,31] Thus, upon irradiation, after the appearance of electron/hole pairs which are generated at the conduction band minimum (CBM) and valence band maximum (VBM), respectively, non-radiative recombination can then be amplified from these defects. For example, Cu^{2+} can easily captures the electron to become Cu$^+$ with full electronic structure, resulting in a bypassing of the W^{6+} to W^{5+} photoredox mechanism. In other example, segregation of the compensating oxygen vacancies at the surface avoids the VB hole/oxygen recombination required to close the photoredox process.

For the bleaching properties, we can first note that many research groups have reported that the bleaching kinetic is very slow for tungsten oxide-based materials. Self-bleaching (when the product is only left in a dark environment to relax) is most often not observed at all; i.e., it is often necessary to heat the film at 80°C–100°C in air or under ozone (oxidative conditions) to obtain a complete relaxation.[2,32] In our case, the three-layered WO and WCu1 films which were previously irradiated for 45 min (to near color saturation) and left in the dark at room temperature for self-bleaching show a photochromic reversibility. The bleaching study was performed in the spectrometer chamber (dark conditions) to record the evolution of the transmission spectra: a spectrum analysis was automatically performed every hour for 20 h, stopping the sample illumination at 500 nm in order to produce any electron/hole pair creation. The absorbance spectra are shown in Fig. 7d and e for WO and WCu1, respectively.

Bleaching evolution was followed, recording the absorbance at 1eV for the WO film and at 0.75 eV for the WCu1 film, in agreement with previous studies. First, for the WO films, the residual absorbance at 1 eV obtained after 20 h of darkening is still important, equal to about 0.3, whereas the bleaching is completed for the WCu1 film, with absorbance equal to 0.02 (Fig. 7f). The absorbance evolution for both films can be fitted from a single exponential decay trend over the entire range of the first 20 h. The single exponential decay function to fit the experimental data, according to Eq. 5, with t and k in hours, is as follows:

$$Y = A_1 \cdot \left[1 - \exp\left(-t/k_1 \right) \right] \tag{5}$$

Comparing the two films (Fig. 7f), the speed of the bleaching mechanism in WCu1 is almost five times that for the WO film: k = 3.09 and 14.05 h, respectively. Thus, copper greatly improved the photochromic reversibility.

Finally, the great bleaching properties observed on copper-doped WO$_3$ film allow cycling tests to be performed. Cycling tests were carried out on the WCu1 film as depicted in Fig. 8. Several irradiation steps were applied for 45 min irradiation, with sufficient darkening duration (15 h, i.e. very close to night/day real cycling conditions) between each irradiation step to let the compound fully self-bleach. The results show that the three cycles are almost identical, which confirms the strong stability of the films under successive cycling, and this augurs well for the application of these thin films as smart windows for environmental buildings.

To briefly summarize, in WO film, the phenomenon of re-oxidation of W^{5+} to W^{6+} by the oxygen in the air is very slow, resulting in a long bleaching time. This represents a severe restriction for large-scale application of such thin films as smart window photochromic films. In WCu1 film, the enhancement in photochromic reversibility, i.e., with a drastic increase in the bleaching kinetic, was ascribed to several factors, based on the characterization results. Notably, the increase in oxygen vacancies in WO$_3$ after Cu doping extended the light-harvesting ability to the visible and NIR regions. Also, the double injection mechanism added to the improved electron interactions thanks to the existence of W^{6+}, W^{5+}, Cu$^+$ and Cu^{2+} ions, which surely plays a significant role in the bleaching improvement. The "de-trapping" of color center electrons created on 5d tungsten orbitals during UV irradiation, thanks to an additional, new W^{5+} - Cu^{2+} → W^{6+} - Cu$^+$ IVCT , is thus proposed. Furthermore, the energetic proximity of the copper 3d (e$_g$) level and oxygen 2p levels, favoring p-d coupling, can further lead to close the photoredox loop through the recombination of the defect electron trapped as Cu$^+$ defect above the VB and the hole created in the maximum of the VB band during irradiation.
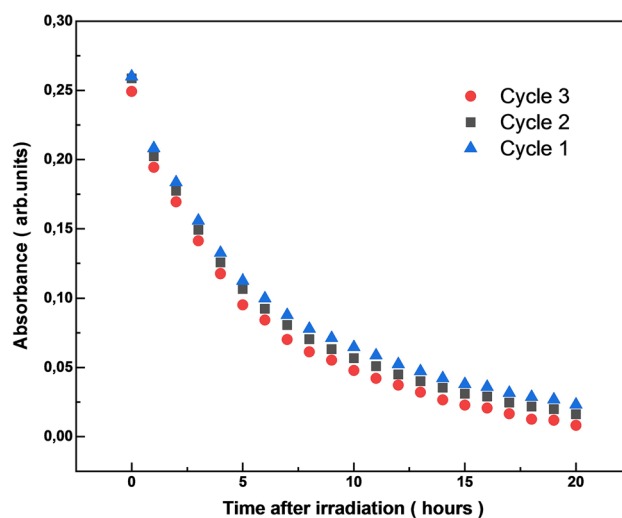

Fig. 8 WCu1 film absorbance evolution at 0.75 eV versus darkening time through three successive coloring/bleaching cycles.

Conclusion

In conclusion, doping of WO_3 with Cu prepared by the polyol method proved to be an effective strategy for improving the bleaching mechanism of our studied films. The photochromism (coloring/bleaching) kinetic of these composites was thoroughly studied. The coloring mechanism of the un-doped films governed mainly by the fast component consists of rapid photoreduction of the surface cations from W^{+6} to W^{+5}; then, after a short time, the surface becomes saturated with W^{+5} ions, and this fast mechanism stops. On the contrary, the WCu1 film kinetic, which is governed by the slow component, corresponds to the ionic diffusion of the W^{5+} from the surface to the material bulk. The WCu1 film records a faster bleaching on the order of 3.09 h compared to 14.05 h for the WO film. The bleaching kinetic was enormously enhanced due to the increase in oxygen vacancies in WO_3 after Cu doping, which in turn extended the light-harvesting ability of this compound to the visible and NIR regions. In addition, the cycling study on WCu1 film confirmed the efficiency of the product in optical applications. This study is proof of the promising utility of our films in different optical applications, such as smart textile, smart window, or optical filters.

Conflict of interest There are no conflicts to declare.

References

1. F. Cora, M. Stachiotti, C.R.A. Catlow, and C.O. Rodriguez, Transition metal oxide chemistry: electronic structure study of WO_3, ReO_3, and $NaWO_3$. *J. Phys. Chem. A* 101, 3945 (1997).

2. J. Wei, X. Jiao, T. Wang, and D. Chen, Electrospun photochromic hybrid membranes for flexible rewritable media. *ACS Appl. Mater. Interfaces* 8, 29713 (2016).

3. R. Diehl, G. Brandt, and E. Salje, The crystal structure of triclinic WO_3. *Acta Crystallogr. A* 34, 1105 (1978).

4. Y.S. Zou, Y.C. Zhang, D. Lou, and H.P. Wang, Structural and optical properties of WO_3 films deposited by pulsed laser deposition. *J. Alloys Compd* 583, 465 (2014).

5. N. Li, Y. Zhao, Y. Wang, Y. Lu, Y. Song, Z. Huang, Y. Li, and J. Zhao, Aqueous synthesis and visible-light photochromism of metastable h-WO_3 hierarchical nanostructures. *Eur. J. Inorg. Chem.* 2015 (17), 2804 (2015).

6. C.S. Blackman, and I.P. Parkin, Atmospheric pressure chemical vapor deposition of crystalline monoclinic WO_3 and WO_{3-x} thin films from reaction of WCl6 with O-containing solvents and their photochromic and electrochromic properties. *Chem. Mater.* 17, 1583 (2005).

7. S.K. Deb, Opportunities and challenges in science and technology of WO_3 for electrochromic and related applications. *Sol. Energy Mater. Sol. Cells* 92, 245 (2008).

8. C.O. Avellaneda, and L.O.S. Bulhones, Photochromic properties of WO_3 and WO_3: X (X=Ti, Nb, Ta and Zr) thin films. *Solid State Ionics* 165, 117 (2003).

9. O. Oderinde, M. Kang, M. Kalulu, F. Yao, and G. Fu, Facile synthesis and study of the photochromic properties of deep eutectic solvent-templated cuboctahedral-WO_3/MoO_3 nanocomposites. *Superlattices Microstruct.* 125, 103 (2018).

10. V. Hariharan, V. Aroulmoji, K. Prabakaran, B. Gnanavel, M. Parthibavarman, R. Sathyapriya, and M. Kanagaraj, Magnetic and electrochemical behaviour of cobalt doped tungsten oxide (WO_3) nanomaterials by microwave irradiation method. *J. Alloys Compd.* 689, 41 (2016).

11. X. Dong, Z. Wu, Y. Guo, Y. Tong, X. Liu, L. Zhang, and Y. Lu, Rational modification in the photochromic and self-bleaching performance of hierarchical microsphere Cu@h-WO_3/WO_3·nH_2O composites. *Solar Energy Mater. Solar Cells* 219, 11078 (2021).

12. Y. Shen, P. Yan, Y. Yang, F. Hu, Y. Xiao, L. Pan, and Z. Li, Hydrothermal synthesis and studies on photochromic properties of Al doped WO_3 powder. *J. Alloy. Compd.* 629, 27 (2015).

13. M. Sun, N. Xu, Y.W. Cao, J.N. Yao, and E.G. Wang, Preparation, microstructure and photochromism of a new nanocrystalline WO_3 film. *J. Mater. Sci. Lett.* 19, 1407 (2000).

14. D.J. Ham, A. Phuruangrat, S. Thongtem, and J.S. Lee, Hydrothermal synthesis of monoclinic WO_3 nanoplates and nanorods used as an electrocatalyst for hydrogen evolution reactions from water. *Chem. Eng. J.* 165, 365 (2010).

15. X. Sun, H. Cao, Z. Liu, and J. Li, Influence of annealing temperature on microstructure and optical properties of sol-gel derived tungsten oxide films. *Appl. Surf. Sci.* 255, 8629 (2009).

16. H. Dong, Y. Chen, and C. Feldmann, Polyol synthesis of nanoparticles: status and options regarding metals oxides, chalcogenides, and non-metal elements. *Green Chem.* 17, 4107 (2015).

17. M. Bourdin, M. Gaudon, F. Weill, M. Duttine, M. Gayot, Y. Messaddeq, and T. Cardinal, Nanoparticles (NPs) of WO_{3-x} compounds by polyol route with enhanced photochromic properties. *Nanomaterials* 9, 1555 (2019).

18. M. Bourdin, G. Salek, A. Fargues, S. Messaddeq, Y. Messaddeq, T. Cardinal, and M. Gaudon, Investigation on the coloring and bleaching processes of WO_{3-x} photochromic thin films. *J. Mater. Chem. C* 8, 9410 (2020).

19. R. Gross, and A. Marx, *"Festkörper physic" 3rd Edition, Hubert & Co* (Göttingen: GmbH & Co. KG, 2018).

20. J.B. Lee, H.J. Le, S.H. Seo, and J.S. Park, Characterization of undoped and Cu-doped ZnO films for surface acoustic wave applications. *Thin Solid Films* 398, 641 (2001).

21. Z. Wang, X. Fan, D. Hana, and F. Gu, Structural and electronic engineering of 3DOM WO_3 by alkali metal doping for improved NO_2 sensing performance. *Nanoscale* 8, 10622 (2016).

22. I.D. Brown, *The chemical bond in inorganic chemistry* (Oxford, U.K.: Oxford University Press, 2002).

23. A.R. West, *Solid State Chemistry and its Applications*, 2nd ed., (New York: John Wiley & Sons, 1991).

24. A. Goldstein, V. Chiriac, and D. Becherescu, On some d^1 Ions Spectra in Oxide Glasses. *J. Non-Cryst. Solids* 92, 271 (1987).

25. D. Möncke, J. Jiusti, L.D. Silva, and A.C.M. Rodrigues, Long-Term stability of laser-induced defects in (fluoride-)phosphate glasses doped with W Mo, Ta, Nb and Zr ions. *J. Non-Crystalline Solids* 498, 401 (2018).

26. H.Y. Wong, C.W. Ong, R.W.M. Kwok, K.W. Wong, S.P. Wong, and W.Y. Cheung, Effects of ion beam bombardment on electrochromic tungsten oxide films studied by x-ray photoelectron spectroscopy and rutherford back-scattering. *Thin Solid Films* 376, 1311 (2000).

27. M. Bourdin, I. Mjejri, A. Rougier, C. Labrugere, T. Cardinal, Y. Messaddeq, and M. Gaudon, Nano-particles (NPs) of WO_3-type

compounds by polyol route with enhanced electrochromic properties. *J. Alloys Compd* 823, 153690 (2020).

28. J. Diaz-Reyes, R. Castillo-Ojeda, M. Galvan-Arellano, and O. Zaca-Moran, Characterization of WO₃ thin films grown on silicon by HFMOD. *Adv. Condens. Matter Phys.* 2013, 591787 (2013).

29. T.H. Fleisch, and G.J. Main, An XPS study of the UV reduction and photochromism of MoO₃ and WO₃. *J. Chem. Phys.* 76, 780 (1982).

30. N. Kadam, T.G. Kim, D.S. Shin, K.M. Garadkar, and J. Park, Morphological evolution of Cu doped ZnO for enhancement of photocatalytic activity. *J. Alloy. Compd.* 710, 102 (2017).

31. B.M. Alshabander, Copper(II)-doped WO₃ nanoparticles with visible light photocatalytic antibacterial activity against gram-positive and gram-negative bacteria. *Inorg. Nano-Met. Chem.* 50 (12), 1329 (2020).

32. S. Wang, W. Fan, Z. Liu, A. Yu, and X. Jiang, Advances on tungsten oxide based photochromic materials: strategies to improve their photochromic properties. *J. Mater. Chem. C* 6, 191 (2018).